Suzuki Yujiro J. (Orcid ID: 0000-0001-7477-1367)
Costa Antonio (Orcid ID: 0000-0002-4987-6471)
Koyaguchi Takehiro (Orcid ID: 0000-0002-4357-1693)

Control of vent geometry on the fluid dynamics of volcanic plumes: insights from numerical simulations

Y.J. Suzuki[1], A. Costa[2], and T. Koyaguchi[1]

[1]Earthquake Research Institute, The University of Tokyo, Tokyo, Japan

[2]Istituto Nazionale di Geofisica e Vulcanologia, Bologna, Italy

Corresponding author: Yujiro J. Suzuki (yujiro@eri.u-tokyo.ac.jp)

Key Points: [Each must be 140 characters]

- Three-dimensional numerical simulations reveal the effects of volcanic vent shape on plume stability and plume height.
- Plumes from narrow fissures are more stable than those from circular vents owing to more efficient dissipation mechanisms near the vent.
- Plume height has complex dependency on vent aspect ratio because of changes in the efficiency of air entrainment.

This article has been accepted for publication and undergone full peer review but has not been through the copyediting, typesetting, pagination and proofreading process which may lead to differences between this version and the Version of Record. Please cite this article as doi: 10.1029/2020GL087038

Plain language summary

Explosive volcanic eruptions eject hot mixtures of gas and ash, forming eruption clouds. Eruption clouds can either become buoyant and rise upward as kilometer-scale volcanic plumes, from which they release ash and gas into the atmosphere, or flow downward along the ground, resulting in devastating pyroclastic flows. Understanding the dynamics of eruption clouds and the critical conditions for generating pyroclastic flows versus volcanic plumes is an important focus of modern volcanology research. We present numerical simulations of eruption clouds using a three-dimensional numerical model to investigate the effects of volcanic vent geometry on plume stability and height. Our simulation results indicate that plume height depends on the shape of the volcanic vent, and can have different dynamics even for the same eruption intensity. These effects of vent shape are caused by the complex mechanism of mixing between the eruption cloud and the ambient air. The efficiency of such mixing inside the cloud largely controls the critical conditions for the generation of pyroclastic flows; above a critical mass flow rate, clouds ejected from circular vents can generate pyroclastic flows, whereas those ejected from thin fissure vents develop stable volcanic plumes.

Abstract

We present three-dimensional numerical simulations of eruption clouds from circular to linear fissure vents to investigate the control of vent shape on the height and stability of volcanic plumes during large explosive eruptions. Our results show that clouds ejected from circular or low-aspect-ratio (nearly-square-like) fissure vents can be associated with radially suspended flow (RSF) at the top of the jet region, whereas those emitted from narrow-fissure vents are not. Non-RSF plumes are more stable than those associated with RSF because the highly concentrated parts of the ejected mixture are easily dissipated and mixed with air near the vent. Plume height in the RSF regime decreases while that in the non-RSF regime increases with increasing aspect ratio, even for a fixed magma flow rate. These observations suggest that the efficiency of air entrainment is influenced by the vent shape, which in turn controls the dynamics of eruption plumes.

Keywords

volcanic plume, vent geometry, plume height, column collapse condition

1. Introduction

Large explosive volcanic eruptions can produce Plinian-type buoyant plumes and/or pyroclastic flows. The hot mixture of volcanic gas and solid pyroclasts that is ejected from the vent entrains ambient air owing to turbulent mixing, significantly reducing its density because the mixed air is heated and expands. When the erupted mixture entrains a small amount of air, the eruption cloud (i.e., the mixture of the fragmented magma, lithics, gas, and entrained air) remains heavier than the ambient air and therefore collapses, resulting in pyroclastic flows. In contrast, when the erupted mixture entrains a large amount of ambient air, the eruption cloud becomes lighter than the surrounding atmosphere and rises, thereby developing a buoyant plume. In the latter scenario, the height of Plinian-type plumes is controlled by the balance between its thermal flux at the vent and the work for lifting up the eruption mixture (and the air from lower altitudes). Therefore, whether the eruption produces buoyant plumes and/or pyroclastic flows, as well as the maximum height of the plume, are strongly controlled by the

amount of air entrained by turbulent mixing (e.g., Cerminara et al., 2016b; Costa et al., 2016; Jessop and Jellinek, 2014; Jessop et al., 2016; Trolese et al., 2019; Woods, 1988).

Some previous studies (Glaze et al., 2011, 2017; Stothers, 1989; Woods, 1993) investigated the effects of vent shape (i.e., circular and linear fissure vents) using simple one-dimensional (1D) models for buoyant plumes (e.g., Morton et al., 1956; Woods, 1988), suggesting that the critical conditions to sustain buoyant plumes is controlled by fissure width. Such studies assume that the amount of entrained air is proportional to characteristic plume velocity at each height and that the efficiency of entrainment (i.e., the entrainment coefficient) has the same constant value for plumes from both circular and fissure vents. However, the entrainment coefficient can be affected by the different turbulent features originated from the different shape of source (Deo et al., 2007a,b; Jessop et al., 2016; Mi et al., 2005; Quinn, 1992; Zaman, 1999) and the local buoyancy at each plume height (Kaminski et al., 2005; Carazzo et al., 2006; Paillat and Kaminski, 2014). In the case of volcanic plumes, the flow features and the local buoyancy are expected to depend on each other. The flow structures, their turbulent features, and the resultant plume heights are controlled by the reversing buoyancy (i.e., from negative to positive buoyancy; e.g., Suzuki et al., 2016b), whereas the magnitude of buoyancy is determined by three-dimensional (3D) structures of volcanic plume. In particular, when the vent radius is large, the dense unmixed part of eruption cloud can generate "fountain-like structure", known as radially suspended flow (RSF; Neri & Dobran, 1994; Suzuki & Koyaguchi, 2012; Suzuki et al., 2016), and its flow structure largely changes stability of eruption column (Suzuki & Koyaguchi, 2012). In order to understand the effects of vent shape on plume dynamics, therefore, it is required to reproduce both of the reversing buoyancy and the 3D flow structures of volcanic plumes.

Examples of large explosive eruptions from linear fissure vents vary from the 1886 eruption from a 17-km-long fissure in Tarawera, New Zealand (Sable et al., 2006; Walker et al., 1984) to the ~100-km-long fissure estimated for the Youngest Toba Tuff super-eruption (Costa & Marti, 2016). In this study, we extend our previous studies (Suzuki and Koyaguchi, 2012; Costa et al., 2018) that investigated the dynamics of plumes from circular vent for large eruptions, and reproduce the fluid dynamics of large eruption clouds from circular to fissure vents using three-dimensional (3D) numerical models. We particularly focus on the effects of vent geometry on plume height and on the conditions for column collapse. We show that the amount of entrained air depends on vent shape, which affects both the peripheral surface of the plume that is first in contact with the ambient air (i.e., the "entrainment area") and the effective value of the entrainment coefficient (i.e., the "entrainment efficiency") associated with different flow structures. The combination of these two effects have a fundamental control on the eruption column dynamics.

2. Methods and model parameters

To investigate the effects of vent shape on eruption cloud dynamics, we numerically simulated circular and fissure vents with different aspect ratios. To quantify the effects of vent shape, we introduced two dimensionless parameters. The first is the aspect ratio of the maximum and minimum dimensions of the vent, $AR = L_{max}/L_{min}$, where L_{max} and L_{min} are the fissure length and width, respectively (following the definition in Mi et al., 2005). The second reflects the deviation of the vent shape from a true circle, $\gamma = 4\pi A/P^2$, where A and P are the vent area and perimeter, respectively. For a given shape (circular or rectangular), γ is a function of AR; γ and AR have a maximum and minimum value, respectively, for $\gamma = AR = 1$ (circular vents), and, for fissure vents, γ decreases as AR increases.

For simplicity, the effects of topography were neglected, assuming the volcanic vent to be located on a flat surface. Furthermore, we assumed that the solid pyroclasts were dynamically and thermodynamically well-coupled with the gas phases (i.e., volcanic gas and entrained air), ignoring particle sedimentation and decoupling (see Cerminara et al., 2016a, 2016b). In the presented models, the transport equations that describe the mass, momentum, and energy conservation as well as the equations of state were solved numerically. The numerical pseudo-gas model was based on the time-dependent solution of the compressible flow Navier-Stokes equations. The model used Implicit LES (ILES) approach where the inherent numerical dissipation act as an implicit subgrid model. We confirmed that when spatial resolution is sufficiently high, both the numerical results with and without the LES approach correctly reproduce the spreading rate of jets observed in the experiments (Suzuki et al., 2005). The simulation results, obtained by the present model, were compared with the other models that used the LES approach (see also the inter-comparison of 3D models in Suzuki et al., 2016a). For the detail of the model, see Suzuki et al. (2005) and Suzuki and Koyaguchi (2013).

The computational domain had a horizontal extent of ~100 km and a vertical extent of ~60 km. Non-uniform structured grids covered the physical domain. The minimum grid cell size was used for the vent and ground surface; it was smaller than $L_{min}/6$, where L_{min} is the minimum length scale of the vent (Table 1). The grid cell size increases with increasing horizontal distance from the crater and with increasing vertical distance from the ground surface. The grid cell size was increased at constant rates of 0.005 and 0.02 units horizontally and vertically, respectively.

A representative tropical atmosphere was used for the initial atmospheric conditions. Atmospheric density and pressure were stratified for a given temperature gradient, and, for simplicity, we assumed calm (i.e., no wind) conditions. We applied no-slip conditions at the ground boundary and free outflow/inflow conditions at the other boundaries. We focused on two eruption intensities with parameters close to the critical condition required for column collapse (Costa et al., 2018). The first eruption type had a mass flow rate (MFR) of 10^9 kg s^{-1}, and the second had an MFR of $10^{9.5}$ kg s^{-1}. The vent exit velocity, temperature, water fraction, and density were set at 256 m s^{-1}, 1053 K, 0.06, and 3.5 kg m^{-3}, respectively (see Costa et al., 2018). Circular and fissure (i.e., rectangular) vent geometries of different dimensions were considered, and the length of the fissure was varied (3.4, 10, and 15 km for MFR = $10^{9.0}$ kg s^{-1}; 10 and 20 km for MFR = $10^{9.5}$ kg s^{-1}). For fixed vent geometry, exit velocity, and magmatic properties, the vent radii and fissure widths can be determined for a given MFR. The input parameters are listed in Table 1.

3. Simulation results

The simulation results show that the flow patterns of volcanic plumes are controlled by the volcanic vent geometry. Here, we describe the simulation results as a function of the *AR* (see Table 1).

For the magmatic properties considered in this study, when the MFR was set as 10^9 kg s^{-1}, the eruption clouds developed stable columns, and did not produce clearly recognizable pyroclastic flows (Fig. 1), regardless of the vent shape. The plumes from circular vents ($\gamma = AR = 1$) were associated with highly concentrated flow of the erupted mixture above the vent (at a height about 4 times the vent diameter), termed "radially suspended flow (RSF)". When the vent radius is large, the erosion by the outer shear layer of the flow does not reach the central axis at the height where the initial momentum is exhausted (defined as H_{mmt}). The dense unmixed cloud stops to rise and spreads radially at this height, resulting in the formation of the RSF.

The large vortices at the top of the RSF entrained a significant amount of ambient air, and the mass fraction of the erupted mixture was significantly reduced in this region (see Supplementary Movies 1 and 2). For a 5-km-long fissure vent (*AR* = 22), the eruption cloud also exhibited RSF structures (Fig. 1b). For high-aspect-ratio fissure vents (*AR* = 91 and 200), a sheet-like buoyant flow (i.e., a quasi-2D vertical flow) developed, and no RSF was observed (Fig. 1c and d; Supplementary Movies 3–4). In these latter cases, the mass fraction of the erupted mixture gradually decreased with height in contrast to the sudden decrease at the top of RSF. Among our simulations, the cases having *AR* from 1 (circular-vent) to 22 belong to the RSF regime, while the cases with high-aspect-ratios (*AR* = 91 or 200) belong to the non-RSF regime.

Changes in plume height over time can reflect the type of flow pattern (Fig. 2a). In runs 1–4 (see Table 1), the height of the plume increased until ~400 s. This period is considered to represent the initial stage of plume development. In the RSF regime (runs 1 and 2), the speed at which the plume increased in height slowed at ~5–10 km at ~100 s but subsequently recovered to the initial conditions. These observations reflect the development of RSF and a rising buoyant plume from the top of the RSF. The height of the plume after 400 s increased as the aspect ratio of the vent increased. The plume height was greater for the fissure vent with a high aspect ratio (run 2; *AR* = 22; *H* = 39–48 km) than for the circular vent (run 1; *AR* = 1; *H* = 35–40 km). In the non-RSF regime (runs 3 and 4), during the developing stage, the rising speed of the plume remained approximately constant. In contrast to the RSF regime, the final height of the plume was observed to decrease as *AR* increases. The plume height was lower when *AR* = 200 (*H* = 38–41 km, run 4) than when *AR* = 91 (*H* = 40–45 km, run 3).

Figure 2b illustrates the vertical distribution of mass fraction of the erupted mixture for the series of simulations with MFR = 10^9 kg s^{-1}. In the RSF regime (runs 1 and 2), the average mass fraction of the erupted mixture was high near the vent (0.9–1.0 in run 1, 0.8–0.9 in run 2). Above the RSF, the mass fraction significantly decreased. The mass concentration in the buoyant region increased as *AR* increased (see also Fig. 1a and b). In the non-RSF regime (runs 3 and 4), the erosion by the outer shear layer reaches the central axis, and the unmixed core disappears at a height (defined as H_{core}) less than H_{mmt}. In this regime the mass concentration decreased gradually with increasing height, but the average mass fraction within the buoyant region remained high (~0.6 for run 3, ~0.3 for run 4). In contrast to the RSF regime, the average mass concentration in the buoyant region was observed to decrease as *AR* increases (Fig. 2b). The observation that plume height increased with increasing mass concentration within the buoyant plume (Fig. 2 and Table 2) is consistent with previous results from 1D models (e.g., Morton et al., 1956).

When the MFR is set at $10^{9.5}$ kg s^{-1}, the volcanic plumes were less stable than those with an MFR value of 10^9 kg s^{-1} (Fig. 1e). For the circular-vent scenario (run 5), a small portion of the ejected mixture was seen to collapse from the top of the RSF, falling to the ground, but the majority of the ejected mixture became buoyant (Fig. 1e; Supplementary Movies 9 and 10). This scenario is indicative of an incipient collapsing regime whereby the collapsing mixture spread on the ground, entrained ambient air, and rose upward where it coalesced with the main buoyant plume (see Costa et al., 2018). For the 10-km-long fissure (run 6; *AR* = 23), the simulated cloud also showed a partial column collapse from the top of the RSF (Fig. 1f; Movies 11 and 12). In contrast, the volcanic plumes from vents with higher aspect ratios (i.e., the 20-km-long fissure, run 7; *AR* =111) were more stable and did not develop RSF structures or pyroclastic flows (Fig. 1g; Supplementary Movies 13 and 14). In this scenario, the plume showed a gradual decrease in mass fraction with increasing height, whereas the plumes in the RSF regime showed the sudden decrease (Fig. 2b).

4. Discussion

In this section, we discuss how vent geometry affects the dynamics of volcanic plumes. Our simulation results indicate that the aspect ratio of the vent (*AR*) significantly affects volcanic plume flow patterns, which in turn controls maximum height and plume stability.

One of the most important controls on the dynamics of volcanic plumes is how the erupted mixture entrains ambient air. The amount of entrained air depends on the entrainment velocity and the peripheral surface area of the plume; the latter directly depends on vent geometry only near the vent, say below the buoyant region. Morton et al. (1956) proposed that the entrainment velocity is proportional to the velocity of a turbulent jet or plume in a uniform environment (i.e., entrainment hypothesis). Some studies have modeled fissure eruptions (Glaze et al., 2011, 2017; Stothers, 1989; Woods, 1993) based on the entrainment hypothesis assuming that the proportionality constant (i.e., entrainment coefficient) itself is independent of vent geometry. In this case, the amount of entrained air depends only on the entrainment area (hence on γ). A small value of γ represents a large entrainment area and $\gamma = 1$ represents the minimum value of the entrainment area. As mentioned above, γ decreases with increasing *AR* (see Table 1).

The fact that for the non-RSF regime, averaged mass concentration in the buoyant region decreases as *AR* increases (Fig. 2b), leading to a decrease in the maximum plume height (Fig. 2a) is consistent with the above assumption that the amount of entrained air below the buoyant region increases as the entrainment area increases. In the RSF regime, however, the mass concentration increases as *AR* increases (Figs 1a, b, and 2b) even though the entrainment area increases (i.e., γ decreases). This is the opposite effect of that observed in the non-RSF regime, suggesting that the entrainment coefficient itself is strongly dependent on the flow pattern and, particularly, the presence of RSF (cf. Koyaguchi et al., 2018).

The critical condition that separates the RSF and non-RSF regimes is determined by the flow geometry near the vent. This condition is the balance between two length scales: (1) the height, where the unmixed core disappears, H_{core}, and (2) the level where the initial momentum is exhausted, H_{mmt} (Koyaguchi et al., 2018; Suzuki & Koyaguchi, 2012). When $H_{\mathrm{core}} < H_{\mathrm{mmt}}$, the highly concentrated core disappears before the initial momentum is exhausted, and the flow is associated with a non-RSF regime. On the other hand, when $H_{\mathrm{core}} > H_{\mathrm{mmt}}$, the highly concentrated core develops RSF at H_{mmt}. It is important to highlight that H_{mmt} is a function of velocity and density of the erupted mixture (i.e., magmatic properties) at the vent and is independent of vent geometry. For our simulations, H_{mmt} is estimated to be 5 km (Fig. S4). In contrast, H_{core} is strongly dependent on vent geometry and is proportional to the vent radius for a circular vent or the minimum length scale of the vent (L_{min}) for a fissure; the value of $H_{\mathrm{core}}/H_{\mathrm{mmt}}$ decreases as *AR* increases (see Fig. S3 and the value of H_{core} in Table 2). As a result, for the high-aspect-ratio scenario (run 7 with *AR* = 111), $H_{\mathrm{core}}/H_{\mathrm{mmt}}$ is so small that a well-mixed buoyant plume, belonging to the non-RSF regime, is generated.

Our results also suggest that column collapse depends on whether the plume belongs to the RSF or non-RSF regime. According to previous studies (e.g., Koyaguchi & Suzuki, 2018; Woods, 1988), column collapse is controlled by the balance of momentum and buoyancy fluxes at the source (i.e., the source Richardson number), and, when the magma properties and exit velocity are fixed as in the present cases, its critical condition is primarily determined by the amount of air entrained in the plume. In the RSF regime, in which a highly concentrated core remains up to H_{mmt} (runs 1 and 2; see Fig. 2b), column collapse is determined by the amount of air entrained within the RSF. In this regime, as the amount of entrained air in the RSF decreases as *AR* increases, the plume is expected to be less stable with increasing *AR*. As *AR* further increases, a transition from an RSF to a non-RSF regime occurs. In the non-RSF

regime (runs 5–7; Fig. 1e–g), the erupted mixture around the central axis of the vent is well-mixed with ambient air, resulting in a steady decrease in density with increasing height, which enhances the stability of the volcanic plume. Unlike the case of the RSF regime, the plume is expected to be more stable with increasing *AR* within this regime. The observed transition from an RSF to non-RSF regime with increasing *AR* provides evidence for a newly identified control of vent geometry on the requirements for column collapse.

The above features associated with the RSF structures cannot be described by 1D models based on the entrainment hypothesis (Morton et al., 1956), since the flow pattern around the RSF is highly complex with a multidimensional structure (Cerminara et al., 2016b; Koyaguchi et al., 2018). However, 1D models are still useful for predicting the stability and height of volcanic plumes if the critical condition between the RSF and non-RSF regimes and the changes in the entrainment efficiency associated with the transition between the two regimes are considered. Suzuki & Koyaguchi (2012) showed that, for circular vents, the critical condition separating the RSF and non-RSF regimes is given by a formula that uses the source Richardson number (eq. 6 in their paper). To apply this formula to fissure eruptions, the effect caused by reduced H_{core}/H_{mmt} due to the minimum length of the vent, L_{min}, should be taken into account; in practice, the vent radius used in the calculation of Richardson number should be replaced with L_{min} (Table 2). Once this Richardson number is introduced, we can discuss the critical condition between the RSF and non-RSF regimes for a wide range of MFR. Our study reveals the opposite dependency of plume height on vent aspect ratio between the RSF and non-RSF regimes. To calculate plume height, future studies need to estimate the effective value of the entrainment coefficient for both the RSF and non-RSF regimes.

The critical condition separating the RSF and non-RSF regimes and that for column collapse can be affected by other factors. The particle decoupling from gas phase can alter the entrainment properties of plumes (e.g., Cerminara et al., 2016b; Jessop and Jellinek, 2014; Jessop et al., 2016). The crater geometry, such as the opening angle of crater, controls the decompression-compression processes and the exit velocity at the crater top (Carcano et al., 2014; Cigala et al., 2017; Kieffer, 1989; Koyaguchi and Suzuki, 2018; Ogden et al., 2008; Woods and Bower, 1995) and the entrainment properties (e.g., Cerminara et al., 2016b; Jessop and Jellinek, 2014). Although these factors may quantitatively change the critical conditions of RSF/non-RSF and stable/collapse regimes, the present results that column collapse depends on whether the plume belongs to the RFS or non-RSF regime as function of the vent shape is considered to be robust because the difference of these regimes is caused by the fundamental features that the clouds are ejected from finite length-scale vent and their buoyancy changes from negative to positive. Finally, further studies should consider how plume dynamics change when magma properties (e.g., temperature, water content) and vent geometries are varied together.

5. Conclusions

Our study showed that vent geometry has two different effects on entrainment process: the peripheral surface of the plume and the flow structure (e.g., the formation of RSF). The combination of these two effects have a fundamental control on the stability and height of volcanic plumes. Volcanic plumes of high mass flow rate from circular or low-aspect-ratio vents are associated with RSF in the lower parts of the plume, near the vent, and are less stable than plumes from high-aspect-ratio vents. For the RSF-type plume, the amount of air within the plume is controlled mainly by the entrainment efficiency around the RSF. The entrainment efficiency decreases and the plume height increases as the aspect ratio increases. In contrast, the amount of ambient air entrained into non-RSF plumes depends on the entrainment area. In

this regime, the entrainment area increases and the plume height decreases as the aspect ratio increases. Column collapse is also critically dependent on whether or not the plumes are associated with RSF.

Acknowledgments

The computations were undertaken mostly using the computer facilities at the Research Institute for Information Technology, Kyushu University, and the Earth Simulator at the Japan Agency for Marine-Earth Science and Technology. Y.J.S. was partially supported by KAKENHI (Grant No. 25750142 and 17K01323) and MEXT "Integrated Program for Next Generation Volcano Research and Human Resource Development". A.C. was partially supported by a grant of the International Research Promotion Office Earthquake Research Institute, the University of Tokyo, and also acknowledge the European project EUROVOLC (grant agreement number 731070) and the MIUR project Premiale Ash-RESILIENCE. Figure 1 was created using the Generic Mapping Tools (GMT) software package. All data for this work are cited in Zenodo (doi:10.5281/zenodo.3603586). The manuscript was improved by comments from Rebecca Carey, David Jessop, Christian Huber, Matteo Cerminara and anonymous two reviewers.

References

Carazzo, G., Kaminski, E., & Tait, S. (2006). The route to self-similarity in turbulent jets and plumes. *Journal of Fluid Mechanics, 547,* 137–148. doi:10.1017/S002211200500683X

Carcano, S., Esposti Ongaro, T., Bonaventura, L, & Neri, A. (2014). Influence of grain-size distribution on the dynamics of underexpanded volcanic jets. *Journal of Volcanology and Geothermal Research, 285,* 60–80. doi:10.1016/j.jvolgeores.2014.08.003

Cerminara, M., Esposti Ongaro, T., & Berselli, L. C. (2016a). ASHEE-1.0 : a compressible, equilibrium-Eulerian model for volcanic ash plumes. *Geosci. Model Dev.*, 9, 697–730. doi:10.5194/gmd-9-697-2016

Cerminara, M., Esposti Ongaro, T., & Neri, A. (2016b). Large eddy simulation of gas-particle kinematic decoupling and turbulent entrainment in volcanic plumes. *Journal of Volcanology and Geothermal Research, 326,* 143–171. doi:10.1016/j.jvolgeores.2016.06.018

Cigala, V., Kueppers, U., Peña Fernández, J. J., Taddeucci, J., Sesterhenn, J., & Dingwell, D. B. (2017). The dynamics of volcanic jets: Temporal evolution of prticles exit velocity from shock-tube experiments. *Journal of Geophysical Research Solid Earth, 122,* 6031–6045. doi:10.1002/2017JB014149

Costa, A., Folch, A., & Macedonio, G. (2013). Density-driven transport in the umbrella region of volcanic clouds: implications for tephra dispersion models. *Geophysical Research Letters, 40,* 4823–4827. doi:10.1002/grl.50942

Costa, A., & Marti J. (2016). Stress field control during large caldera-forming eruptions, *Frontiers of Earth Science, 4,* 92. doi:10.3389/feart.2016.00092

Costa, A., Suzuki, Y. J., Cerminara, M., Devenish, B. J., Esposti Ongaro, T., Herzog, M., Van Eaton, A. R., Denby, L. C., Bursik, M., de'Michieli Vitturi, M., Engwell, S., Neri, A., Barsotti, S., Folch, A., Macedonio, G., Girault, F., Carazzo, G., Tait, S., Kaminski, E., Mastin, L. G., Woodhouse, M. J., Phillips, J. C., Hogg, A. J., Degruyter, W., & Bonadonna, C. (2016). Results of the eruptive column model inter-comparison study. *Journal of Volcanology and Geothermal Research, 326,* 2–25. doi:10.1016/j.jvolgeores.2016.01.017

Costa, A., Suzuki, Y. J., & Koyaguchi, T. (2018). Understanding the plume dynamics of explosive super-eruptions. *Nature Communications, 9*:654. doi:10.1038/s41467-018-02901-0

Deo, R. C., Mi, J., & Nathan, G. J. (2007a). The influence of nozzle aspect ratio on plane jets. *Experimental Thermal and Fluid Science, 31*, 825–838. doi:10.1016/j.expthermflusci.2006.08.00

Deo, R. C., Mi, J., & Nathan, G. J. (2007b). The influence of nozzle-exit geometric profile on statistical properties of a turbulent plane jet. *Experimental Thermal and Fluid Science, 32*, 545–559. doi:10.1016/j.expthermflusci.2007.06.004

Glaze, L. S., Baloga, S. M., & Wimert, J. (2011). Explosive volcanic eruptions from linear vents on Earth, Venus, and Mars: Comparisons with circular vent eruptions. *Journal of Geophysical Research, 116*, E01011. doi:10.1029/2010JE003577

Glaze, L. S., Self, S., Schmidt, A., & Hunter, S. J. (2017). Assessing eruption column height in ancient flood basalt eruptions. *Earth and Planetary Science Letters, 457*, 263–270. doi:10.1016/j.epsl.2014.07.043

Jessop, D. E., & Jellinek, A. M., (2014). Effects of particle mixtures and nozzle geometry

on entrainment into volcanic jets. *Geophysical Research Letters, 41*, 3858–3863. doi:10.1002/2014GL060059

Jessop, D. E., Gilchrist, J., Jellinek, A. M., & Roche, O. (2016). Are eruptions from linear fissures and caldera ring dykes more likely to produce pyroclastic flows? *Earth and Planetary Science Letters, 454*, 142–153. doi:10.1016/j.epsl.2016.09.005

Kaminski, E., Tait, S., & Carazzo, G. (2005). Turbulent entrainment in jets with

arbitrary buoyancy. *Journal of Fluid Mechanics, 526*, 361–376. doi: 10.1017/S0022112004003209

Kieffer, S. W. (1989). Geologic nozzles, *Reviews of Geophysics, 27*, 3–38. doi: 10.1029/RG027i001p00003

Koyaguchi, T., & Suzuki, Y. J. (2018). The condition of eruption column collapse: 1. A reference model based on analytical solutions. *Journal of Geophysical Research: Solid Earth, 123*. doi:10.1029/2017JB015308

Koyaguchi, T., Suzuki, Y. J., Takeda, K., & Inagawa, S. (2018) The condition of eruption column collapse: 2. Three-dimensional numerical simulations of eruption column dynamics. *Journal of Geophysical Research: Solid Earth, 123*. doi:10.1029/2017JB015259

Mi, J., Deo, R. C., & Nathan, G. J. (2005). Characterization of turbulent jets from high-aspect-ratio rectangular nozzles. *Physics of Fluids, 17*, 068102. doi: 10.1063/1.1928667

Morton, B. R., Taylor, G., & Turner, J. S. (1956). Turbulent gravitational convection from maintained and instantaneous sources. *Proceedings of the Royal Society of London, A234*, 1–23. doi:10.1098/rspa.1956.0011

Neri, A., & Dobran, F. (1994). Influence of eruption parameters on the thermofluid dynamics of collapsing volcanic columns. *Journal of Geophysical Research, 99*(B6), 11,833–11,857. doi:10.1029/94JB00471

Ogden, D. E., Wohletz, K. H., Glatzmaier, G. A., & Brodsky, E. E. (2008). Numerical simulations of volcanic jets: Importance of vent overpressure. *Journal of Geophysical Research, 113*, B02204. doi:10.1029/2007JB005133

Paillat, S., & Kaminski, E. (2014). Entrainment in plane turbulent pure plumes. *Journal of Fluid Mechanics, 775*, R2. doi:10.1017/jfm.2014.424

Quinn, W. R. (1992). Turbulent free jet flows issuing from sharp-edges rectangular slots: The influence of slot aspect ratio. *Experimental Thermal and Fluid Science, 5*, 203–215. doi:10.1016/0894-1777(92)90007-R

Sable, J. E., Houghton, B. F., Wilson, C. J. N., & Carey, R. J. (2006). Complex proximal sedimentation from Plinian plumes: the example of Tarawera 1886. *Bulletin of Volcanology, 69*, 89–103. doi:10.1007/s00445-006-0057-6

Stothers, R. B. (1989). Turbulent atmospheric plumes above line sources with an application to volcanic fissure eruptions on the terrestrial planets. *Journal of the Atmospheric Sciences, 46(17)*, 2662–2670. doi:10.1175/1520-0469(1989)046<2662:TAPALS>2.0.CO;2

Suzuki, Y. J., Costa, A., Cerminara, M., Esposti Ongaro, T., Herzog, M., Van Eaton, A. R., & Denby, L. C. (2016a). Inter-comparison of three-dimensional models of volcanic plumes. *Journal of Volcanolgy and Geothermal Research, 326*, 26 – 42. doi:10.1016/j.jvolgeores.2016.06.011

Suzuki, Y. J., Costa, A., & Koyaguchi, T. (2016b). On the relationship between eruption intensity and volcanic plume height: Insights from three-dimensional numerical simulations. *Journal of Volcanology and Geothermal Research, 326*, 120–126. doi:10.1016/j.jvolgeores.2016.04.016.

Suzuki, Y. J., & Koyaguchi, T. (2012). 3-D numerical simulations of eruption column collapse: Effects of vent size on pressure-balanced jet/plumes. *Journal of Volcanology and Geothermal Research, 221–222*, 1–13. doi:10.1016/j.jvolgeores.2012.01.013

Suzuki, Y. J., & Koyaguchi, T. (2013). 3D numerical simulation of volcanic eruption clouds during the 2011 Shinmoe-dake eruptions. *Earth, Planets and Space, 65*, 581–589. doi:10.5047/eps.2013.03.009

Suzuki, Y. J., Koyaguchi, T., Ogawa, M., & Hachisu, I. (2005). A numerical study of turbulent mixing in eruption clouds using a three-dimensional fluid dynamics model. *Journal of Geophysical Research, 110*, B08201. doi:10.1029/2004JB003460

Trolese, M., Cerminara, M., Esposti Ongaro, T., & Giordano, G. (2019) The footprint of column collapse regimes on pyroclastic flow temperatures and plume heights. Nature *Nature Communications, 10*:2476. doi:10.1038/s41467-019-10337-3

Walker, G. P. L., Self, S., & Wilson, L. (1984). Tarawera 1886, New Zealand–A basaltic Plinian fissure eruption. *Journal of Volcanology and Geothermal Research, 21*, 61–78. doi:10.1016/0377-0273(84)90016-7

Woods, A. W. (1988). The fluid dynamics and thermodynamics of eruption columns. *Bulletin of Volcanology, 50*(3), 169–193. doi:10.1007/BF01079681

Woods, A. W. (1993). A model of the plumes above basaltic fissure eruptions. *Geophysical Research Letters, 20*(12), 1115–1118. doi:10.1029/93GL01215

Woods, A. W., & Bower, S. M. (1995). The decompression of volcanic jets in a crater during explosive volcanic eruptions. *Earth and Planetary Science Letters, 131*, 189–205. doi:10.1016/0012-821X(95)00012-2

Zaman, K B. M. Q. (1999). Spreading characteristics of compressible jets from nozzles of various geometries. 383, 197–228. doi:10.1017/S0022112099003833

Table 1. Input parameters for the simulations

Run	MFR (kg s^{-1})	Vent geometry	L_{max} (km)	L_{min} (km)	AR L_{max}/L_{min}	γ $4\pi A/P^2$	ΔX_{min} (km)	ΔX_{max} (km)
1	10^9	Circle	1.2	1.2	1	1.00	0.060	0.30
1hr	10^9	Circle	1.2	1.2	1	1.00	0.030	0.15
2	10^9	Fissure	3.4	0.33	10	0.26	0.033	0.30
3	10^9	Fissure	10	0.11	91	0.034	0.014	0.11
4	10^9	Fissure	15	0.075	200	0.016	0.013	0.15
5	$10^{9.5}$	Circle	2.2	2.2	1	1.00	0.11	0.30
6	$10^{9.5}$	Fissure	10	0.36	28	0.10	0.044	0.30
7	$10^{9.5}$	Fissure	20	0.18	111	0.028	0.030	0.18

MFR: Mass Flow Rate, L_{max}: Maximum length scale, L_{min}: Minimum length scale, AR: the aspect ratio, γ: the deviation of the vent shape from a true circle, ΔX_{min}: Minimum grid size, ΔX_{max}: Maximum grid size.

Table 2. Summary of simulation results

Run	Ri(L_0)	Ri(L_{min})	RSF/non-RSF	Stable/Collapse	H_{max} (km)	H_{core} (km)
1	0.18	0.18	RSF	Stable	33–40	5.2
2	0.18	0.049	RSF	Stable	40–46	7.2
3	0.18	0.017	non-RSF	Stable	50–55	1.2
4	0.18	0.011	non-RSF	Stable	48–51	0.9
5	0.31	0.31	RSF	Collapse	40–46	5.2
6	0.31	0.052	RSF	Stable	42–45	7.0
7	0.31	0.026	non-RSF	Stable	45–49	3.0

Ri(L_0), Ri(L_{min}) : Richardson number based on L_0 and L_{min}, respectively. H_{max} is the maximum plume height estimated from time average for 600–800 s in Fig. 2a. H_{core} was estimated from the highest level where the mass fraction of the erupted mixture is 0.9 in Figure S3.

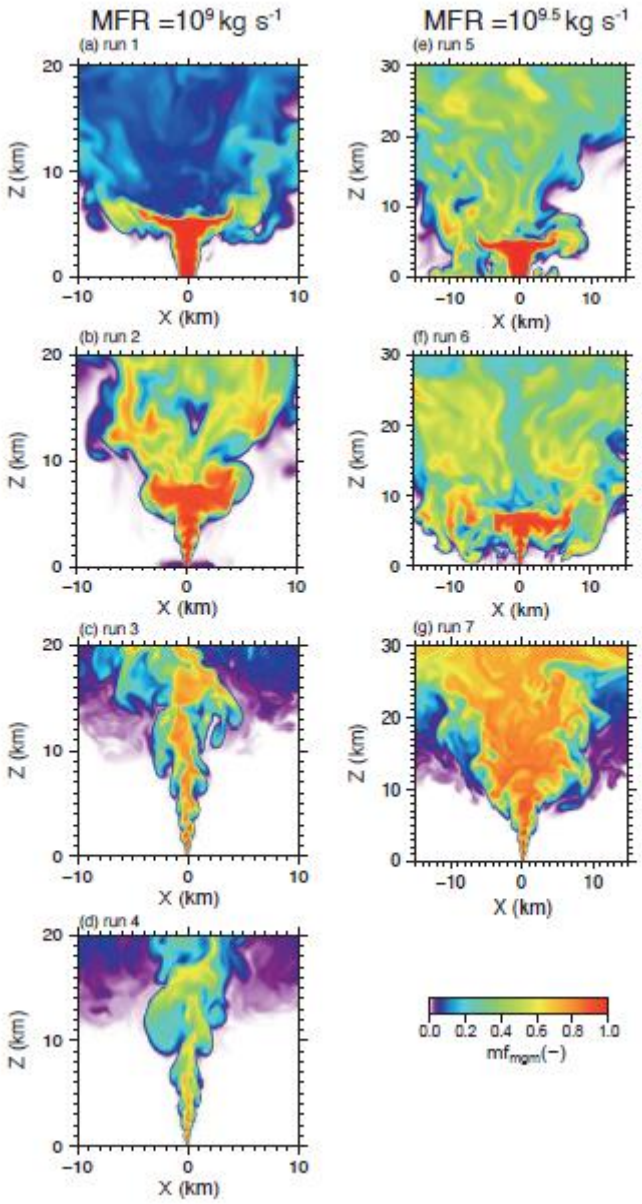

Figure 1. Simulation results for plumes with two Mass Flow Rates (a–d: 10^9 kg s^{-1}, e–g: $10^{9.5}$ kg s^{-1}) and varied vent geometry (a, e: circular vent, b–d, f, g: fissure vent). The panels show vertical cross-sections (y = 0 km) of the mass fraction of the erupted mixture (mf_{mgm}) at t = 800 s. The initial conditions of the vent in each run are listed in Table 1**.**

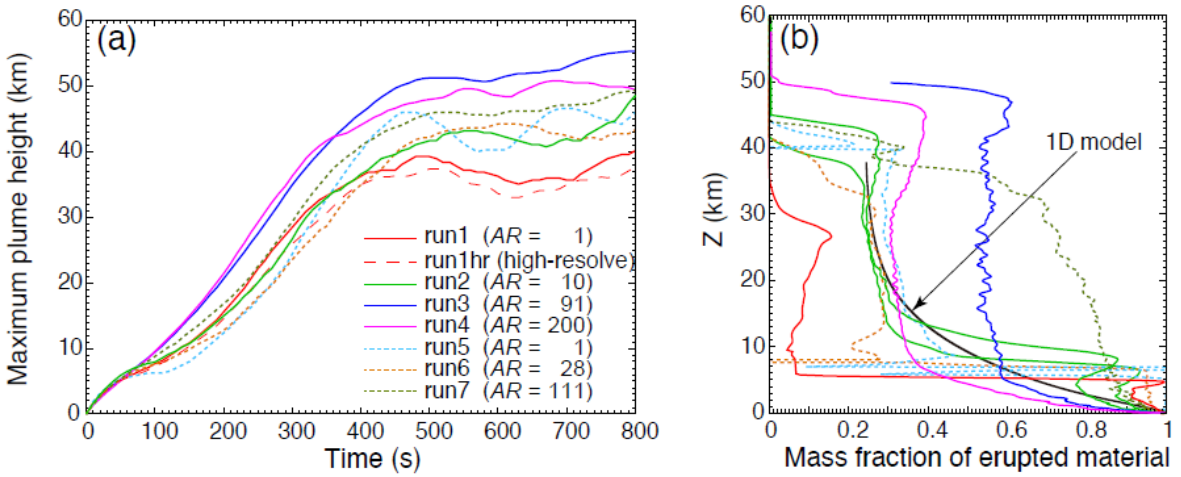

Figure 2. (a) Maximum height as a function of time. (b) Vertical profiles of the mass fraction of the erupted mixture around the central axis of the vent for the different simulations, using the filter for horizontal averaging (f3 in Suzuki et al. (2016a)). The heights in (a) were estimated using the maximum levels where the mass fraction of the erupted mixture is 0.01. The solid curves represent the results for 10^9 kg s^{-1}, whereas the dashed ones represent those for $10^{9.5}$ kg s^{-1}. The simulation result of run 1hr (high resolution) with high spatial resolutions show qualitatively similar features as that of run 1. The time window used to compute averages in (b) is 600–800 s. The black curve represents the result of the 1D model (Woods, 1988).